A Framework for Unsupervised Segmentation of Lung Tissues from Low Dose Computed Tomography Images

Ayman El-Baz[1], Georgy Gimel'farb[2], Robert Falk[3],
Trevor Holland[1], and Teresa Shaffer[1]

[1]Bioimaging Laboratory, Bioengineering Department,
University of Louisville, Louisville, KY, USA.
[2] Department of Computer Science, University of Auckland,
Auckland, New Zealand.
[3]Director, Medical Imaging Division, Jewish Hospital,
Louisville, KY, USA.

Abstract

New techniques for more accurate unsupervised segmentation of lung tissues from Low Dose Computed Tomography (LDCT) are proposed. In this paper we describe LDCT images and desired maps of regions (lung and the other chest tissues) by a joint Markov-Gibbs random field model (MGRF) of independent image signals and interdependent region labels but focus on most accurate model identification. To better specify region borders, each empirical distribution of signals is precisely approximated by a Linear Combination of Discrete Gaussians (LCDG) with positive and negative components. We modify a conventional Expectation-Maximization (EM) algorithm to deal with the LCDG and develop a sequential EM-based technique to get an initial LCDG-approximation for the modified EM algorithm. The initial segmentation based on the LCDG-models is then iteratively refined using a MGRF model with analytically estimated potentials. Experiments on real data sets confirm high accuracy of the proposed approach.

1 Introduction

Lung Cancer remains the leading cause of cancer-related deaths in the US. In 2006, there were approximately 174,470 new cases of lung cancer and 162,460 related deaths [1]. Early diagnosis of cancer can improve the effectiveness of treatment and increase the patient's chance of survival. Segmentation of the lung tissues is a crucial step for early detection and diagnosis of lung nodules. Accurate segmentation of lung tissues from LDCT images is a challenging problem because some lung tissues such as arteries, veins, bronchi, and bronchioles are very close to the chest tissues. Therefore, the segmentation cannot be based only on image signals but have to account also for spatial relationships between the region labels in order to preserve the details of the lung region.
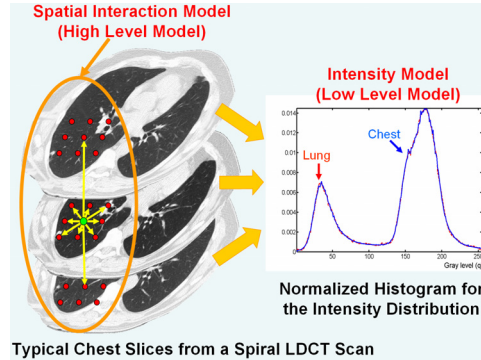
Figure 1: Illustration of joint Markov-Gibbs model of LDCT lung images.

In the literature, there are many techniques developed for lung segmentation in CT images. Sluimer et al. [2] presented a survey on computer analysis of the lungs in CT scans. This survey addressed segmentation of various pulmonary structures, registration of chest scans, and their applications. Hu et al. [3], proposed an optimal gray level thresholding technique which is used to select a threshold value based on the unique characteristics of the data set. A segmentation-by-registration scheme was proposed by Sluimer et al. [4] for automated segmentation of the pathological lung in CT. For more on lung segmentation techniques, refer, e.g., to the survey by Sluimer et al. [2].

In this paper we describe LDCT images and desired maps of regions by a joint Markov-Gibbs random field model (MGRF) of independent image signals and interdependent region labels but focus on most accurate model identification. To better specify region borders, each empirical distribution of signals is precisely approximated by a Linear Combination of Discrete Gaussians (LCDG) with positive and negative components. Approximation of an empirical relative frequency distribution of scalar data with a particular probability density function is widely used in pattern recognition and image processing, e.g., for data clustering or image segmentation [5]. The basic problem is to accurately approximate, within the data range, not only the peaks, or modes of the probability density function for the measurements but also its behavior between the peaks.

2 Joint Markov-Gibbs model of LDCT lung images

Let $\mathbf{R} = \{(i,j,z) : 1 \leq i \leq I, 1 \leq j \leq J, 1 \leq z \leq Z\}$ denote a finite arithmetic grid supporting grayscale LDCT images $\mathbf{g} : \mathbf{R} \to \mathbf{Q}$ and their region maps $\mathbf{m} : \mathbf{R} \to \mathbf{X}$. Here, $\mathbf{Q} = \{0, \ldots, Q-1\}$ and $\mathbf{X} = \{1, \ldots, X\}$ are the sets of gray levels and region labels, respectively, where Q is the number of gray levels and X is the number of image classes to separate by segmentation.

The MGRF model of images to segment is given by a joint probability distribution of LDCT images and desired region maps $P(\mathbf{g}, \mathbf{m}) = P(\mathbf{m})P(\mathbf{g}|\mathbf{m})$. Here, $P(\mathbf{m})$ is an unconditional distribution of maps and $P(\mathbf{g}|\mathbf{m})$ is a conditional distribution of images, given a map. The Bayesian MAP estimate of the map, given the image $\mathbf{g}$, $\mathbf{m}^* = \arg\max_{\mathbf{m}} L(\mathbf{g}, \mathbf{m})$

maximizes the log-likelihood function:

$$L(\mathbf{g},\mathbf{m}) = \log P(\mathbf{g}|\mathbf{m}) + \log P(\mathbf{m}) \tag{1}$$

In this work we focus on accurate identification of the spatial interaction between the lung voxels ($P(\mathbf{m})$) and the intensity distribution for the lung tissues ($P(\mathbf{g}|\mathbf{m})$) as shown in Fig. 1.

2.1 Spatial interaction model of LDCT images

Generic Markov-Gibbs model of region maps [6] that accounts for only pairwise interactions between each region label and its neighbors has generally an arbitrary interaction structure and arbitrary Gibbs potentials identified from image data. For simplicity, we restrict the interactions to the nearest voxels (26-neighborhood) and assume, by symmetry considerations, that the interactions are independent of relative region orientation, are the same for all classes, and depend only on intra- or inter-region position of each voxel pair (i.e. whether the labels are equal or not). Under these restrictions, the model is similar to the conventional auto-binomial ones [6] and differs only in that the potentials are not related to a predefined function and have analytical estimates.

The symmetric label interactions are three-fold: the closest horizontal-vertical-diagonal in the current slice (hvdc), the closest horizontal-vertical-diagonal in the upper slice (hvdu), and the closest horizontal-vertical-diagonal in the lower slice (hvdl). The potentials of each type are bi-valued because only coincidence or difference of the labels are taken into account. Let $\mathbf{V}_a = \{V_a(x,\chi) = V_{a,\text{eq}}$ if $x = \chi$ and $V_a(x,\chi) = V_{a,\text{ne}}$ if $x \neq \chi$: $x,\chi \in \mathbf{X}\}$ denote bi-valued Gibbs potentials describing symmetric pairwise interactions of type $a \in \mathbf{A} = \{\text{hvdc},\text{hvdu},\text{hvdl}\}$ between the region labels. Let $\mathbf{N}_{\text{hvdc}} = \{(1,0,0),(0,1,0),(-1,0,0),(0,-1,0)\}$, $\mathbf{N}_{\text{hvdu}} = \{(0,0,1),(-1,-1,1),(-1,1,1),(1,-1,1),(1,1,1)\}$, and $\mathbf{N}_{\text{hvdl}} = \{(0,0,-1),(-1,-1,-1),(-1,1,-1),(1,-1,-1),(1,1,-1)$ be subsets of inter-voxel offsets for the 26-neighborhood system. Then the Gibbs probability distribution of region maps is as follows:

$$P(\mathbf{m}) \propto \exp\left(\sum_{(i,j,z)\in\mathbf{R}}\sum_{a\in\mathbf{A}}\sum_{(\xi,\eta,\zeta)\in\mathbf{N}_a} V_a(m_{i,j,z},m_{i+\xi,j+\eta,z+\zeta})\right) \tag{2}$$

To identify the MGRF model described in Eq. (2), we have to estimate the Gibbs Potentials $\mathbf{V}$. In this paper we introduce a new analytical maximum likelihood estimation for the Gibbs potentials[1].

$$V_{a,\text{eq}} = \frac{X^2}{X-1}\left(f_a'(\mathbf{m}) - \frac{1}{X}\right) \quad \text{and} \quad V_{a,\text{ne}} = \frac{X^2}{X-1}\left(f_a''(\mathbf{m}) - 1 + \frac{1}{X}\right) \tag{3}$$

where $f_a'(\mathbf{m})$ and $f_a''(\mathbf{m})$ denote the relative frequency of the equal and non-equal pairs of the labels in all the equivalent voxel pairs $\{((i,j,z),(i+\xi,j+\eta,z+\zeta)): (i,j,z) \in \mathbf{R}.; (i+\xi,j+\eta,z+\zeta) \in \mathbf{R}; (\xi,\eta,\zeta) \in \mathbf{N}_a\}$, respectively.

---

[1]The proof is provided on our web site: http://uofl.edu/speed/bioengineering/faculty/bioengineering-full/dr-ayman-el-baz/elbazlab.html.

2.2 Intensity model of LDCT lung images

Let q; $q \in \mathbf{Q} = \{0, 1, \ldots, Q - 1\}$, denote the Q-ary gray level. The discrete Gaussian is defined as the probability distribution $\Psi_\theta = (\psi(q|\theta) : q \in \mathbf{Q})$ on $\mathbf{Q}$ such that $\psi(q|\theta) = \Phi_\theta(q + 0.5) - \Phi_\theta(q - 0.5)$ for $q = 1, \ldots, Q - 2$, $\psi(0|\theta) = \Phi_\theta(0.5)$, $\psi(Q - 1|\theta) = 1 - \Phi_\theta(Q - 1.5)$ where $\Phi_\theta(q)$ is the cumulative Gaussian function with a shorthand notation $\theta = (\mu, \sigma^2)$ for its mean, μ, and variance, σ^2.

We assume the number K of dominant modes, i.e. regions, objects, or classes of interest in a given LDCT images, is already known. In contrast to a conventional mixture of Gaussians and/or other simple distributions, one per region, we closely approximate the empirical gray level distribution for LDCT images with an LCDG having C_p positive and C_n negative components such that $C_p \geq K$:

$$p_{\mathbf{w},\theta}(q) = \sum_{r=1}^{C_p} w_{p,r} \psi(q|\theta_{p,r}) - \sum_{l=1}^{C_n} w_{n,l} \psi(q|\theta_{n,l}) \tag{4}$$

under the obvious restrictions on the weights $\mathbf{w} = [w_{p,.}, w_{n,.}]$: all the weights are non-negative and

$$\sum_{r=1}^{C_p} w_{p,r} - \sum_{l=1}^{C_n} w_{n,l} = 1 \tag{5}$$

To identify the LCDG-model including the numbers of its positive and negative components, we modify the EM algorithm to deal with the LCDG.

First, the numbers $C_p - K$, C_n and parameters $\mathbf{w}$, θ (weights, means, and variances) of the positive and negative DG components are estimated with a sequential EM-based initializing algorithm. The goal is to produce a close initial LCDG-approximation of the empirical distribution. Then under the fixed C_p and C_n, all other model parameters are refined with an EM algorithm that modifies the conventional one in [7] to account for the components with alternating signs.

2.2.1 Sequential EM-based initialization:

Sequential EM-based initialization forms an LCDG-approximation of a given empirical marginal gray level distribution using the conventional EM-algorithm [7] adapted to the DGs. At the first stage, the empirical distribution is represented with a mixture of K positive DGs, each dominant mode being roughly approximated with a single DG. At the second stage, deviations of the empirical distribution from the dominant K-component mixture are modeled with other, "subordinate" components of the LCDG. The resulting initial LCDG has K dominant weights, say, $w_{p,1}, \ldots, w_{p,K}$ such that $\sum_{r=1}^{K} w_{p,r} = 1$, and a number of subordinate weights of smaller values such that $\sum_{r=K+1}^{C_p} w_{p,r} - \sum_{l=1}^{C_n} w_{n,l} = 0$.

The subordinate components are determined as follows. The positive and negative deviations of the empirical distribution from the dominant mixture are separated and scaled up to form two new "empirical distributions". The same conventional EM algorithm is iteratively exploited to find the subordinate mixtures of positive or negative DGs that approximate best the scaled-up positive or negative deviations, respectively. The sizes $C_p - K$ and C_n of these mixtures are found by sequential minimization of the total absolute error between each scaled-up deviation and its mixture model by the number of the components. Then the obtained positive and negative subordinate models are scaled down and then added to the dominant mixture yielding the initial LCDG model.

2.2.2 Modified EM algorithm for LCDG:

Modified EM algorithm for LCDG maximizes the log-likelihood of the empirical data by the model parameters assuming statistically independent signals:

$$L(\mathbf{w}, \theta) = \sum_{q \in \mathbf{Q}} f(q) \log p_{\mathbf{w}, \theta}(q) \tag{6}$$

A local maximum of the log-likelihood in Eq. (6) is given with the EM process extending the one in [7] onto alternating signs of the components. Let $p_{\mathbf{w}, \theta}^{[m]}(q) = \sum_{r=1}^{C_p} w_{p,r}^{[m]} \psi(q | \theta_{p,r}^{[m]}) - \sum_{l=1}^{C_n} w_{n,l}^{[m]} \psi(q | \theta_{n,l}^{[m]})$ denote the current LCDG at iteration m. Relative contributions of each signal $q \in \mathbf{Q}$ to each positive and negative DG at iteration m are specified by the respective conditional weights

$$\pi_p^{[m]}(r|q) = \frac{w_{p,r}^{[m]} \psi(q | \theta_{p,r}^{[m]})}{p_{\mathbf{w}, \theta}^{[m]}(q)}; \quad \pi_n^{[m]}(l|q) = \frac{w_{n,l}^{[m]} \psi(q | \theta_{n,l}^{[m]})}{p_{\mathbf{w}, \theta}^{[m]}(q)} \tag{7}$$

such that the following constraints hold:

$$\sum_{r=1}^{C_p} \pi_p^{[m]}(r|q) - \sum_{l=1}^{C_n} \pi_n^{[m]}(l|q) = 1; \; q = 0, \ldots, Q-1 \tag{8}$$

The following two steps iterate until the log-likelihood changes become small:

E– step$^{[m+1]}$: Find the weights of Eq. (7) under the fixed parameters $\mathbf{w}^{[m]}$, $\theta^{[m]}$ from the previous iteration m, and

M– step$^{[m+1]}$: Find conditional MLEs $\mathbf{w}^{[m+1]}$, $\theta^{[m+1]}$ by maximizing $L(\mathbf{w}, \theta)$ under the fixed weights of Eq. (7).

Considerations closely similar to those in [7] show this process converges to a local log-likelihood maximum. Let the log-likelihood of Eq. (6) be rewritten in the equivalent form with the constraints of Eq. (8) as unit factors:

$$L(\mathbf{w}^{[m]}, \theta^{[m]}) = \sum_{q=0}^{Q} f(q) \left[\sum_{r=1}^{C_p} \pi_p^{[m]}(r|q) \log p^{[m]}(q) - \sum_{l=1}^{C_n} \pi_n^{[m]}(l|q) \log p^{[m]}(q) \right] \tag{9}$$

Let the terms $\log p^{[m]}(q)$ in the first and second brackets be replaced with the equal terms $\log w_{p,r}^{[m]} + \log \psi(q | \theta_{p,r}^{[m]}) - \log \pi_p^{[m]}(r|q)$ and $\log w_{n,l}^{[m]} + \log \psi(q | \theta_{n,l}^{[m]}) - \log \pi_n^{[m]}(l|q)$, respectively, which follow from Eq. (7). At the E-step, the conditional Lagrange maximization of the log-likelihood of Eq. (9) under the Q restrictions of Eq. (8) results just in the weights $\pi_p^{[m+1]}(r|q)$ and $\pi_n^{[m+1]}(l|q)$ of Eq. (7) for all $r = 1, \ldots, C_p$; $l = 1, \ldots, C_n$ and $q \in \mathbf{Q}$. At the M-step, the DG weights $w_{p,r}^{[m+1]} = \sum_{q \in \mathbf{Q}} f(q) \pi_p^{[m+1]}(r|q)$ and $w_{n,l}^{[m+1]} = \sum_{q \in \mathbf{Q}} f(q) \pi_n^{[m+1]}(l|q)$ follow from the conditional Lagrange maximization of the log-likelihood in Eq. (9) under the restriction of Eq. (5) and the fixed conditional weights of Eq. (7). Under these latter, the conventional MLEs of the parameters of each DG stem

from maximizing the log-likelihood after each difference of the cumulative Gaussians is replaced with its close approximation with the Gaussian density (below "c" stands for "p" or "n", respectively):

$$\mu_{c,r}^{[m+1]} = \frac{1}{w_{c,r}^{[m+1]}} \sum_{q \in \mathbf{Q}} q \cdot f(q) \pi_c^{[m+1]}(r|q)$$

$$(\sigma_{c,r}^{[m+1]})^2 = \frac{1}{w_{c,r}^{[m+1]}} \sum_{q \in \mathbf{Q}} \left(q - \mu_{c,i}^{[m+1]}\right)^2 \cdot f(q) \pi_c^{[m+1]}(r|q)$$

This modified EM-algorithm is valid until the weights $\mathbf{w}$ are strictly positive. The iterations should be terminated when the log-likelihood of Eq. (6) does not change or begins to decrease due to accumulation of rounding errors.

The final mixed LCDG-model $p_C(q)$ is partitioned into the K LCDG-submodels $P_{[k]} = [p(q|k) : q \in \mathbf{Q}]$, one per class $k = 1, \ldots, K$, by associating the subordinate DGs with the dominant terms so that the misclassification rate is minimal.

The whole iterative segmentation process is as follows:

- ○ **Initialization:** Find an initial map by the voxelwise Bayesian MAP classification of a given LDCT image after initial estimation of X LCDG-models of signals of each object class represented by one of the dominant modes.

- ○ **Iterative refinement:** Refine the initial map by iterating these two steps:

  1. Estimate the potential values for region map model using Eq. (3).
  2. Re-collect the empirical gray level densities for the current regions, re-approximate these densities, and update the map.
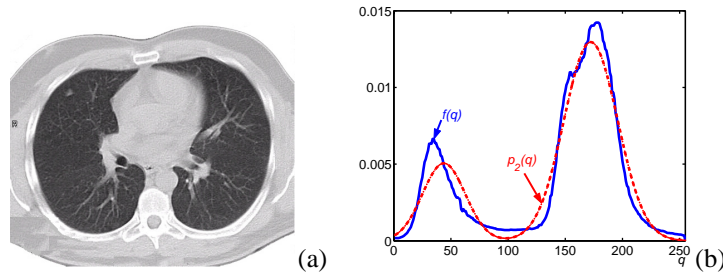

(a)   (b)

Figure 2: Typical LDCT scan slice (a) and the empirical distribution $f(q)$ and the estimated dominant 2-component mixture $p_2(q)$ (b).

3   Experimental Results and Validation

Experiments were conducted with the Low Dose Computed Tomography (LDCT) images acquired with a multidetector GE Light Speed Plus scanner (General Electric, Milwuakee, USA) with the following scanning parameters: slice thickness of 2.5 mm reconstructed every 1.5 mm, scanning pitch 1.5, 140 KV, 100 MA, and F.O.V 36 cm. The
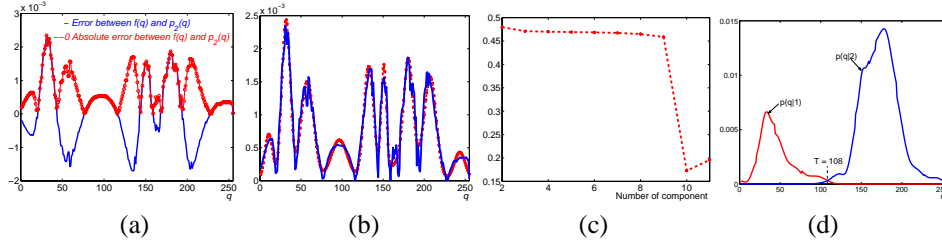
Figure 3: Deviations and absolute deviations between $f(q)$ and $p_3(q)$ (a), the mixture model (b) of the absolute deviations in (a), the absolute error (c) as a function of the number of Gaussians approximating the scaled-up absolute deviations in (a), and the initial estimated LCDG-models for each class (d).
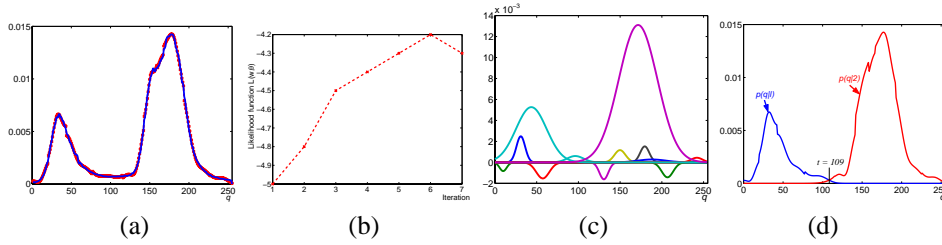

Figure 4: Final 2-class LCDG-model overlaying the empirical density (a), the log-likelihood dynamics (b) the LCDG model components (c), and the estimated density for each class using LCDG-models (d).

size of each 3D data set is $512 \times 512 \times 182$. The LDCT images contain two classes ($K = 2$), namely, darker lung tissues and brighter chest region. A typical LDCT slice, its empirical marginal gray level distribution $f(q)$, and the initial 2-component Gaussian dominant mixture $p_2(q)$ are shown in Fig. 2. Figure 3 illustrates basic stages of our sequential EM-based initialization by showing the scaled-up alternating and absolute deviations $f(q) - p_2(q)$, the best mixture model estimated for the absolute deviations (these ten Gaussian components give the minimum approximation error), and the initial LCDG-models for each class. Figure 4 presents the final estimated LCDG-model using the proposed modified EM-algorithm. The final LCDG of each class are obtained with the best separation threshold $t = 109$ as shown in Fig 4(d).

The region map obtained first with only the class LCDG-models is further refined using the iterative segmentation algorithm. Changes in the likelihood $L(\mathbf{g}, \mathbf{m})$ become very small after 12 iterations. For this map the initial estimated parameters are $V_{a,eq} = -V_{a,ne} = 1.02$, and the final estimated parameters are $V_{a,eq} = -V_{a,ne} = 1.67$. The final region map produced with these parameters using the Metropolis voxelwise relaxation is shown in Fig. 5. For comparison, Fig. 5 presents also the initial region map, the map refined with the randomly selected potentials, segmentation obtained by MRS algorithm [8], segmentation obtained by ICM algorithm [9], and the "ground truth" segmentation done by a radiologist. More 3D segmentation results are shown in Fig. 6. In order to better measure
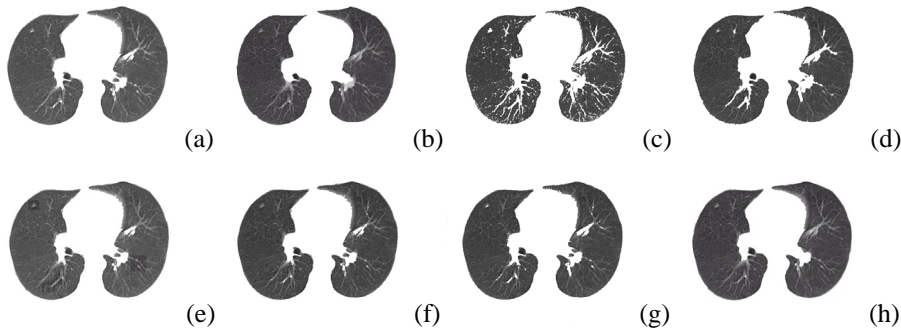
Figure 5: Initial (a) and final (b) segmentation by the proposed approach (the final error 1.1% comparing to the ground truth); initial (c) and final (d) segmentation using the conventional normal mixture obtained by the EM algorithm (the final error 5.1%); refined lung regions (e) obtained from (a) using the randomly chosen Gibbs potentials of the map model (the final error 1.8%); (f) best segmentation obtained by the MRS algorithm with the potential values 0.3 and three level of resolution (error 2.3%); (g) best segmentation obtained by the ICM algorithm with the potential values 0.3 (error 2.9%), and the ground truth (h) produced by a radiologist.

the accuracy of our approach, we have created a geometric phantom with the same gray level distribution in regions as in the CT slices at hand. The phantom, its ideal region map, and results of our segmentation are shown in Fig. 7. The error 0.09% between the found regions and ground truth confirms the high accuracy of the proposed segmentation techniques. For comparison, Fig. 7 shows also the segmentation obtained with the iterative thresholding (IT) approach, the ICM algorithm [9], the MRS algorithm [8], the deformable model which uses the tractional gradient-based external force [10], and the more advanced deformable model using the GVF [11].

The above experiments, as well as additional experiments with 1820 different bimodal LDCT slices, have shown that our segmentation yields much better results than several more conventional algorithms. As indicated in Table 1, the most accurate algorithm among these latter algorithms, namely, the MRS [8], has the larger error range of $1.9 - 9.8\%$ the mean error of 5.1% with respect to the ground truth. Our segmentation has the notably smaller error range of $0.1 - 2.15\%$ and its mean error of 0.32% is more than fifteen times less.

4   Conclusions

Our experiments show that the proposed accurate identification of the Markov–Gibbs random field model demonstrates promising results in segmenting the lung region from LDCT images. The main difference with respect to more conventional schemes is in the use of precise LCDG-models to approximate signal distributions and analytical estimates of the MGRF parameters. The proposed segmentation techniques include (*i*) the accurate sequential initialization to form a starting LCDG-model, (*ii*) the modified EM algorithm
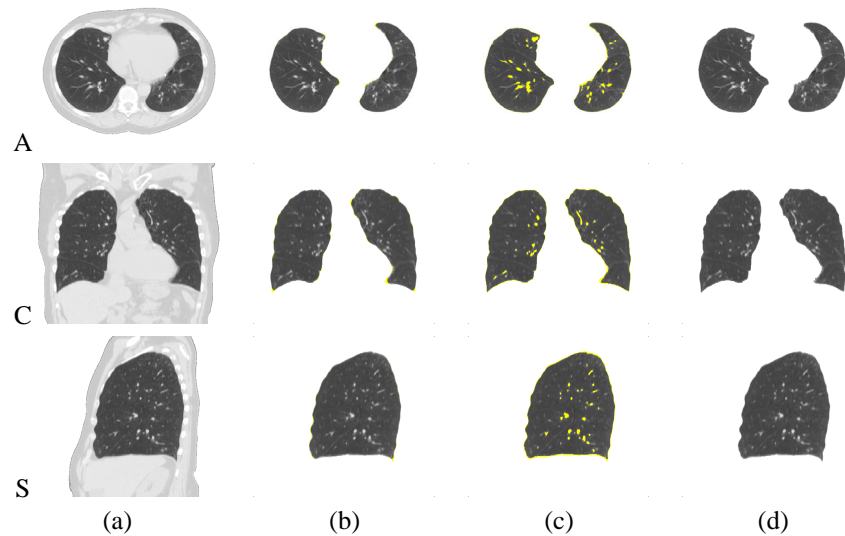
Figure 6: Results of 3D Lung segmentation projected onto 2D axial (A), coronal (C), and saggital (S) planes for visualization: 2D profiles of the original LDCT images (a), our segmentation (b), IT segmentation, and (d) the radiologist's segmentation. Note that our segmentation errors are only around the outer edge (Error 0.79%. and the IT-based segmentation error is 4.57%. The errors are highlighted by yellow color.
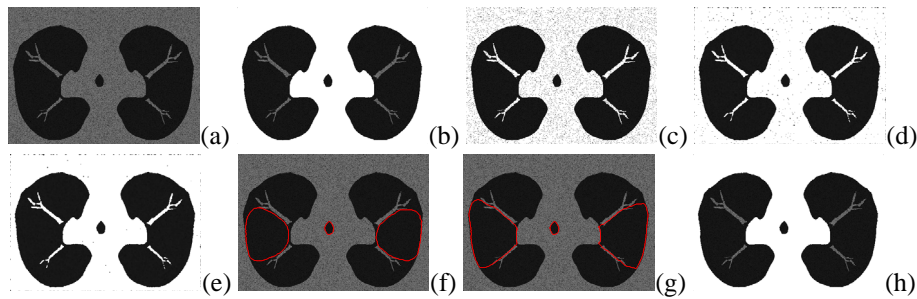

Figure 7: Generated phantom (a), its lung regions segmented with our approach (b; the error 0.09%), the IT approach (c; the error 5.97%), the ICM algorithm (d; the least error 2.91% obtained with the potential values 0.3); the MRS algorithm (e; the error 1.98% with the potential values 0.3 and three resolution levels), the deformable model using the traditional image gradient as an external force (f; the error 59.4%), the deformable model with the gradient vector field as an external force (g; the error 51.9%), and the ground truth (h).

for refining the starting model, and (*iii*) the iterative map refinement using the identified conditional MGRF model. Our present implementation on C++ programming language

Table 1: Accuracy of our segmentation in comparison to five algorithms (IT, MRS [8], ICM [9], the gradient-based deformable model DMG [10], and the deformable model based on the gradient vector flow GVF [11]).

Error, %	Segmentation algorithm					
	Our	IT	MRS	ICM	DMG	GVF
Minimum	**0.1**	2.81	1.90	2.03	10.1	4.10
Maximum	**2.15**	21.9	9.80	17.1	29.1	18.2
Mean	**0.32**	10.9	5.10	9.80	15.1	13.2
St.dev.	**0.71**	6.04	3.31	5.11	7.77	4.81
Significance less than		10^{-4}	10^{-3}	10^{-4}	10^{-4}	10^{-4}

on the Intel quad processor (3.2GHz each) with 16 GB memory and 2 TB hard drive with RAID technology takes about 296 sec for processing 182 LDCT slices of size 512×512 pixels each, i.e about 1.65 sec per slice.

References

[1] American Cancer Society: Cancer Facts and Figures (2006).

[2] I. Sluimer, A. Schilham, M. Prokop, and B. van Ginneken, "Computer analysis of computed tomography scans of the lung: a survey," *IEEE TMI*, vol. 25, no. 4, pp. 385–405, 2006.

[3] S. Hu, E. Hoffman, and J. Reinhardt, "Automatic lung segmentation for accurate quantitation of volumetric x-ray ct images," *IEEE TMI*, vol. 20, pp. 490–498, 2001.

[4] I. Sluimer, M. Prokop, and B. van Ginneken, "Toward automated segmentation of the pathological lung in CT," *IEEE TMI*, vol. 24, no. 8, pp. 1025–1038, 2005.

[5] R. Duda, P. Hart, and D. Stork, *Pattern Classification,* 2nd ed., Wiley: New York, 2001.

[6] G. Gimel'farb, *Image textures and Gibbs random fields,* Kluwer Academic: Dordrecht, 1999.

[7] M. Schlesinger and V. Hlavac, *Ten Lectures on Statistical and Structural Pattern Recognition*, Kluwer Academic, Dordrecht, 2002.

[8] C. Bouman and B. Liu, "Multiple resolution segmentation of textured images", *IEEE Trans. Pattern Analysis Machine Intelligence*, vol. 13, pp. 99–113, 1991.

[9] J. Besag, "On the statistical analysis of dirty pictures", *J. Royal Statistical Society*, vol. B48, pp. 259–302, 1986.

[10] M. Kass, A. Witkin, and D. Terzopoulos, "Snakes: Active contour models,"*Int. J. Computer Vision*, vol. 1, pp. 321–331, 1987.

[11] C. Xu and J. Prince, "Snakes, shapes, and gradient vector flow," *IEEE Trans. Pattern Analysis Machine Intelligence*, vol. 7, pp. 359–369, 1998.